catalysts

MDPI

Article

High-Performance Bifunctional HER/OER Electrocatalysis Enabled by Solvothermal Cobalt Growth on Screen-Printed Nickel Microparticle Interlayers

Ioannis Poimenidis [1,*], Bochenek Kamil [2,3], Martsinchyk Aliaksandr [3], Majewska Karolina [3], Shuhayeu Pavel [3], Jarosław Milewski [3] and Michalis Konsolakis [1,*]

[1] Lab of Materials Science and Processes, School of Production Engineering & Management, Technical University of Crete, 73100 Chania, Crete, Greece
[2] Institute of Fundamental Technological Research, Polish Academy of Sciences, Pawińskiego 5B, 02-106 Warsaw, Poland; kamil.bochenek@pw.edu.pl
[3] Faculty of Power and Aeronautical Engineering, Warsaw University of Technology, 21/25 Nowowiejska Street, 00-665 Warsaw, Poland; jaroslaw.milewski.phd@gmail.com (J.M.)
* Correspondence: ipoimenidis@tuc.gr (I.P.); mkonsolakis@tuc.gr (M.K.)

Abstract

For efficient alkaline water-splitting, it is crucial to have bifunctional electrocatalysts that exhibit low overpotentials, durability, and the possibility of being produced through scalable methods. This study involved the use of screen printing to apply a porous nickel microparticle/polymer interlayer onto commercial nickel foam, which then acted as a base for the solvothermal growth of cobalt-based oxide/hydroxide nanostructures. The optimized electrode showed excellent bifunctional capabilities in 1 M KOH, requiring only 61 mV for the hydrogen evolution reaction and 241 mV for the oxygen evolution reaction at a current density of 10 mA cm^{-2}. In comparison, the control electrodes, such as those with cobalt directly deposited on unmodified nickel foam and screen-printed nickel foam substrates without cobalt, exhibited poorer overall performance. Although the cobalt-modified nickel foam exhibited a higher C_{dl}-derived apparent electrochemical surface area, the cobalt-modified screen-printed electrode achieved the best ECSA-normalized HER and OER responses, indicating that the enhancement in activity was not solely due to the capacitive surface area of the electrode. The increased integrated redox charge suggests a greater contribution from electrochemically accessible Co/Ni redox-active species, while impedance analysis supports a more favorable apparent interfacial response under the tested HER- and OER-relevant conditions. Long-term chronopotentiometry and post-stability SEM confirmed stable bifunctional operation.

Keywords: alkaline water splitting; bifunctional electrocatalyst; HER/OER; nickel foam; screen printing

Academic Editors: Junhu Wang and Ganeshraja Ayyakannu Sundaram

Received: 21 June 2026
Revised: 16 July 2026
Accepted: 21 July 2026
Published: 23 July 2026

1. Introduction

The development of efficient, durable, and low-cost electrocatalysts for alkaline water splitting remains a central challenge in the field of sustainable hydrogen production. Water electrolysis offers a direct route for converting renewable electricity into high-purity hydrogen; however, its large-scale implementation is still limited by the kinetic barriers associated with the hydrogen evolution reaction (HER) and, more critically, the oxygen evolution reaction (OER). Recent advances in electrochemical energy catalysis further emphasize that

catalyst architecture, active-site accessibility, and efficient electron/ion transport are critical for improving HER and OER performance in practical water-electrolysis systems [1,2]. Although noble-metal-based catalysts, such as Pt for HER and Ir/Ru oxides for OER, exhibit excellent activity, their prohibitive cost and rarity restrict their practical applications [3–5]. Therefore, the design of earth-abundant bifunctional electrocatalysts capable of promoting both HER and OER at low overpotentials and with long-term operational stability is of considerable importance.

Among non-noble transition metal-based systems, cobalt-containing oxides and hydroxides have attracted significant attention owing to their rich redox chemistry, tunable oxidation states, and favorable catalytic properties in alkaline media [6–8]. In particular, Co-based materials can participate in reversible Co^{2+}/Co^{3+} redox transitions and generate hydroxylated surface species relevant to water dissociation, interfacial charge transfer, and OER-related surface reconstruction [9,10]. Under alkaline OER conditions, Co-based oxide surfaces may reconstruct toward CoOOH-like oxyhydroxide species, which are frequently considered the catalytically relevant phase [1]. The effectiveness of cobalt-based electrocatalysts in practical applications is influenced by factors other than their inherent chemical makeup. It also relies on how well they are structurally integrated with the current collector, the availability of electroactive sites, and the durability of the catalyst/support interface during operations that produce gas [10].

Nickel foam is widely used as a three-dimensional conductive substrate for alkaline electrocatalysis because of its high electrical conductivity, open macroporous architecture, mechanical robustness, and compatibility with the growth of transition metal oxides/hydroxides [11,12]. The interconnected design of the porous network enhances the penetration of electrolytes and the release of gases, making it particularly appealing for electrodes used in water splitting at high current densities [13]. However, the direct application of active materials onto nickel foam may result in uneven catalyst distribution, inadequate interfacial attachment, partial obstruction of macropores, and ineffective use of the deposited active phase [14]. These limitations highlight the need for substrate-engineering strategies that can improve catalyst nucleation, adhesion, and electrochemical accessibility without compromising the conductivity of open-cell foams [15].

Applying intermediate functional layers to nickel foam surfaces offers a promising solution to these challenges. Within this framework, screen printing stands out because of its scalability, affordability, compatibility with patterned deposition, and suitability for creating porous coatings over extensive electrode surfaces [16–18]. A screen-printed nickel microparticle layer can introduce additional roughness, local porosity, and metallic contact points, thereby modifying the nucleation environment for subsequent catalyst growth [16–18]. Unlike dense or insulating coatings, a properly designed nickel-based interlayer can preserve electrical conductivity while increasing the number of anchoring sites available for solvothermal deposition. However, the role of such screen-printed metallic interlayers in controlling cobalt-based bifunctional HER/OER electrodes has not been elucidated sufficiently.

In this study, a bifunctional alkaline water-splitting electrode was developed by integrating screen printing and solvothermal cobalt growth on commercial Ni foam. In a previous study, we successfully enhanced a supercapacitor using this approach [18]. Initially, a porous nickel microparticle/polymer interlayer was deposited onto nickel foam via screen printing, resulting in a modified substrate referred to as NF-m. This interlayer served as a scaffold for the solvothermal formation of cobalt-based oxide/hydroxide nanostructures, culminating in the fabrication of the Co@NF-m electrode. The design aims to augment the geometric roughness of the nickel foam while establishing a structurally inte-

grated conductive framework. This framework facilitates cobalt growth, improves catalyst anchoring, and enhances the electrochemical utilization of Co/Ni redox-active sites.

The fabricated electrodes were systematically evaluated using structural, morphological, surface chemical, and electrochemical characterizations techniques. The Co@NF-m electrode exhibited superior bifunctional performance in 1 M KOH, requiring low overpotentials of 61 and 241 mV for the HER and OER, respectively, at 10 mA cm^{-2} current density. Importantly, although Co@NF exhibited a higher C_{dl}-derived apparent electrochemical surface area, Co@NF-m delivered stronger ECSA-normalized HER and OER responses, indicating that the improved activity cannot be attributed solely to a larger capacitive surface area. Instead, the integrated redox-charge analysis and impedance response suggest a more effective participation of electrochemically accessible Co/Ni redox-active species and a more favorable apparent interfacial electrochemical response. Long-term chronopotentiometric measurements further confirmed the operational robustness of the optimized electrode under both HER and OER conditions, while post-stability SEM analysis showed the preservation of a porous morphology without severe delamination. These findings demonstrate that screen-printed nickel microparticle interlayers can serve as effective structural platforms for engineering robust transition metal-based bifunctional electrocatalysts for alkaline water-splitting.

2. Results and Discussion

2.1. Structural and Morphological Characterization

The morphology, crystalline structure, and surface chemical composition of the fabricated electrodes were systematically examined to clarify the role of the screen-printed interlayer in the subsequent formation of the Co active phase. The screen-printed NF substrate (NF-m) was developed by implementing a porous nickel microparticle interlayer on commercial nickel foam via screen printing. This modification was intended to enhance the surface roughness, promote cobalt growth, and improve the mechanical integration of the subsequently deposited cobalt species.

The SEM images in Figure 1a–d reveal clear morphological differences among the investigated electrodes. The NF-m substrate preserved the open macroporous structure of the pristine nickel foam, as shown in the inset of Figure 1a, and introduced a rough particulate surface composed of Ni microparticles. This rough architecture provides additional anchoring sites for the solvothermal growth of cobalt-based species. After cobalt deposition, Co@NF-m exhibited a dense and relatively homogeneous coverage of interconnected cobalt-based nanostructures on the modified foam surface (Figure 1b,c). The resulting hierarchical morphology combines the macroporous conductive framework of nickel foam with a rough Ni interlayer and nanoscale Co-containing features, which is expected to improve the electrolyte penetration and increase the number of accessible electroactive sites, as discussed below. In comparison, Co@NF prepared directly on pristine nickel foam displays a more compact surface morphology with larger agglomerated regions (Figure 1d), suggesting that the screen-printed interlayer significantly influences cobalt growth and promotes a more structurally integrated active layer.

The elemental composition was further supported by EDS analysis (Table 1). The NF-m substrate was mainly composed of Ni with a minor O contribution, which can be attributed to the native surface oxide/hydroxide layer formed upon exposure to air. After cobalt deposition, both Co@NF and Co@NF-m showed the presence of Co, O, and Ni, confirming the successful formation of cobalt-containing surface layers. For Co@NF-m, the detectable Ni signal indicated that the Co-based layer remained porous and did not completely block the underlying metallic framework. In contrast, the lower Ni signal observed for Co@NF suggests a more continuous cobalt-rich coverage on the pristine NF.

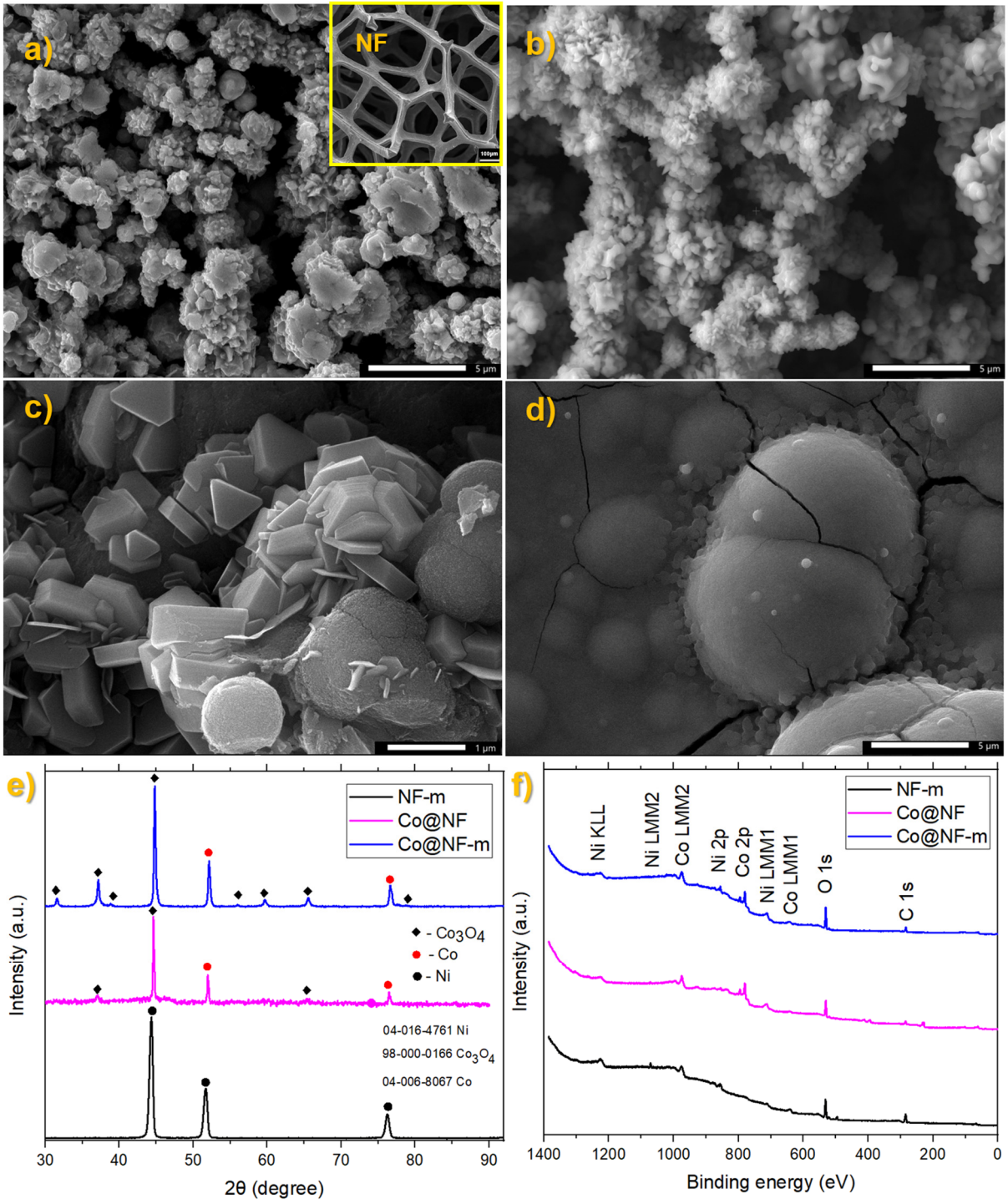

Figure 1. SEM images of the fabricated electrodes: NF-m and pristine NF (inset) (**a**), Co@NF-m (**b**,**c**), and Co@NF (**d**). The XRD patterns (**e**) and XPS survey spectra (**f**) verify the presence of Ni, Co, O, and C species on the modified electrodes.

Table 1. EDS-derived elemental compositions of the NF-m, Co@NF-m, and Co@NF electrodes, expressed as mass and atomic percentages.

Electrode	O Mass %	Co Mass %	Ni Mass %	O Atomic %	Co Atomic %	Ni Atomic %
NF-m	1.58 ± 0.1	—	98.42 ± 1.0	5.55 ± 0.3	—	94.45 ± 1.0
Co@NF-m	21.52 ± 0.4	54.91 ± 0.8	23.57 ± 0.5	50.22 ± 0.8	34.79 ± 0.5	14.99 ± 0.4
Co@NF	25.34 ± 0.4	72.00 ± 0.9	2.66 ± 0.2	55.55 ± 0.8	42.86 ± 0.5	1.59 ± 0.1

XRD was employed to examine the crystalline structures of the electrodes, as shown in Figure 1e. The NF-m substrate exhibited the characteristic reflections of face-centered cubic metallic Ni at $2\theta \approx 44.5^\circ$, 51.8°, and 76.4°, assigned to the (111), (200), and (220) planes, respectively. The absence of additional crystalline phases indicates that the screen-printing modification preserved the metallic Ni framework of the catalyst. After cobalt deposition, additional diffraction peaks appeared at approximately $2\theta \approx 19.0^\circ$, 31.3°, 36.8°, 44.8°, 59.3°, and 65.2°, which were indexed to the (111), (220), (311), (400), (511), and (440) planes of spinel Co_3O_4, respectively. These reflections confirm the formation of crystalline cobalt oxide on both Co-deposited electrodes.

The crystallite size of Co@NF-m was estimated using the Scherrer equation from the selected XRD reflections, as summarized in Table S1. The Co_3O_4 crystallite size calculated from the intense (311) reflection at $2\theta \approx 36.8^\circ$ was approximately 21.7 nm, confirming the nanocrystalline nature of the deposited cobalt oxide. The estimated values for the Ni(111) and Co-related reflections were approximately 16.3 nm and 24.9 nm, respectively. The formation of nanoscale Co_3O_4 domains is beneficial for HER/OER electrocatalysis because it shortens the ion diffusion pathways and increases the density of electrochemically accessible active sites [19–21].

The surface chemical composition was evaluated using XPS survey analysis, as shown in Figure 1f. The survey spectra confirmed the presence of Ni, Co, O, and C species on the modified electrodes, verifying the successful deposition of cobalt-based species onto the Ni foam substrates. The Ni signal originated from the metallic nickel foam/interlayer and surface-oxidized nickel species, whereas the Co and O signals were associated with the cobalt oxide/hydroxide surface layer. The C 1s contribution was mainly attributed to adventitious carbon and/or residual carbon-containing surface species.

High-resolution XPS spectra were used to clarify the oxidation states of the surface species (Figures S1–S3). The Ni 2p spectra of NF-m, Co@NF-m, and Co@NF show characteristic Ni^{2+} $2p_{3/2}$ and Ni^{2+} $2p_{1/2}$ components, along with satellite features, indicating the presence of surface-oxidized nickel species. The Co 2p spectra of Co@NF and Co@NF-m displayed Co $2p_{3/2}$ and Co $2p_{1/2}$ peaks accompanied by satellite features, consistent with the mixed Co^{2+}/Co^{3+} states in cobalt oxide. This mixed-valence configuration is important for alkaline electrocatalysis because it can support reversible surface redox transitions and charge transfer [22,23]. Because of the pronounced multiple splitting and overlapping shake-up satellite contributions, exact Co^{3+}/Co^{2+} and Ni^{3+}/Ni^{2+} ratios were not extracted, and the spectra were interpreted conservatively as evidence of heterogeneous oxide/hydroxide surface environments. The hydroxyl-related surface contributions of Co@NF and Co@NF-m were comparable, with only a slightly higher relative M-OH contribution for Co@NF-m. This result supports the presence of hydroxylated, redox-active cobalt-containing surface species on both electrodes, while indicating that the superior activity of Co@NF-m cannot be attributed solely to a higher surface hydroxyl content. The screen-printed Ni microparticle interlayer appears to play a primary structural and electrochemical role by modifying the surface architecture and promoting more effective accessibility and utilization of the deposited Co-based phase, as supported by the redox charge and impedance results (see below). The hydroxyl-related component is particularly relevant because surface M-OH species can participate in water dissociation, interfacial redox reactions, and OER-related surface reconstruction [24,25]. Moreover, possible Ni-Co interfacial electronic effects cannot be excluded, but they are not conclusively asserted because direct spectroscopic evidence of a specific charge-transfer interaction is unavailable.

2.2. Electrochemical Evaluation

The electrochemical behavior of the NF-m, Co@NF, and Co@NF-m electrodes was first examined by cyclic voltammetry in 1 M KOH. As shown in Figure 2a, Co@NF-m exhibited a larger CV envelope than both Co@NF and NF-m within the investigated potential window, indicating a stronger overall electrochemical response. Since this potential region includes Co-based surface redox/Faradaic processes, the enlarged CV area of Co@NF-m suggests the enhanced participation of electrochemically accessible cobalt redox sites rather than a purely capacitive contribution. To avoid interference from the anodic OER current, the redox-charge analysis was performed exclusively on the cathodic branch of the CV profiles recorded at 10 mV s^{-1}, using a common potential window of 1.00–1.40 V vs. RHE. A linear local baseline was subtracted before the numerical integration. The quantitative integration of the baseline-subtracted cathodic profiles further supports this interpretation, showing that Co@NF-m possesses an approximately 3.65-fold higher cathodic redox charge than Co@NF, indicating a larger apparent contribution from the electrochemically accessible Co/Ni redox-active species (Tables 2 and S3; Figure S5). Because the integrated charge of a defined redox process is proportional to the amount of electrochemically participating redox species, the higher the baseline-subtracted cathodic charge of Co@NF-m the greater the apparent redox participation under identical integration conditions. However, owing to overlapping Co/Ni redox transitions and the uncertainty in the effective electron-transfer number, this quantity is used only as a comparative descriptor of redox accessibility and active-phase utilization, as detailed in Section S4 of the Supplementary Materials.

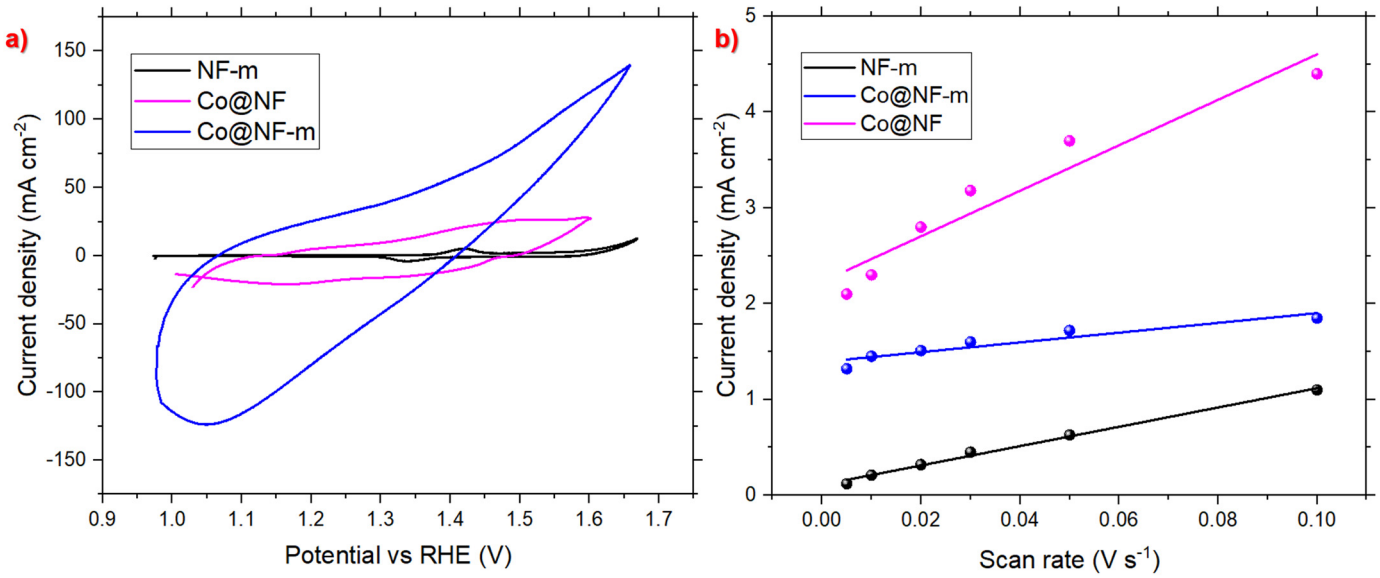

Figure 2. (**a**) CV at 10 mV s^{-1} in 1 M KOH, and (**b**) linear relationship between the average capacitive current density and scan rate, obtained from non-faradaic CV measurements, for C_{dl} estimation of the NF-m, Co@NF, and Co@NF-m electrodes.

Table 2. C_{DL}, ECSA values, and relative baseline-subtracted cathodic redox charges of the NF-m, Co@NF, and Co@NF-m electrodes.

Electrode	C_{dl} (mF cm^{-2})	Apparent ECSA Factor	Relative Baseline-Subtracted Cathodic Active Charge
NF-m	10.9 ± 0.4	272.5	0.09
Co@NF	23.7 ± 1.3	592.5	1.00
Co@NF-m	7.2 ± 0.7	180	3.65

To separate the capacitive contribution from the faradaic processes, the double-layer capacitance was estimated from the CV measurements recorded in a non-faradaic potential region at different scan rates (Figure S4). The average capacitive current density was plotted as a function of the scan rate, as shown in Figure 2b. The calculated C_{dl} values were 10.9 ± 0.4, 23.7 ± 1.3, and 7.2 ± 0.7 mF cm^{-2} for NF-m, Co@NF, and Co@NF-m, respectively. The corresponding ECSA values, summarized in Table 2, were estimated according to Equation (1):

$$ECSA = C_{dl}/C_s, \quad (1)$$

where C_s is the specific capacitance of an ideally smooth electrode surface, which is commonly taken as 40 μF cm^{-2} [26]. Based on this approximation, Co@NF exhibited the highest C_{dl}-derived ECSA, followed by NF-m and Co@NF-m.

Interestingly, the C_{dl}-derived ECSA trend did not follow the trend observed in the wider faradaic CV window. Although Co@NF exhibited the largest apparent capacitive surface area, Co@NF-m displayed the strongest redox response and the highest cathodic redox charge. This distinction indicates that the C_{dl}-derived ECSA should be considered an apparent electrochemical surface descriptor rather than a direct measure of the number or catalytic efficiency of the Co active sites [27]. The superior activity of Co@NF-m is likely related to the more effective integration of the Co-based active phase with the screen-printed NF-m interlayer, which promotes a higher population of electrochemically accessible redox-active sites. Furthermore, as discussed below, Co@NF-m maintained the highest HER and OER responses, even after ECSA normalization. This indicates that the improved bifunctional performance was not governed solely by the apparent capacitive surface area of the material.

The bifunctional electrocatalytic activity of the NF-m, Co@NF, and Co@NF-m electrodes was further evaluated for HER and OER in 1 M KOH. The HER polarization curves are shown in Figure 3a, while the corresponding Tafel plots are presented in Figure 3b. Among the examined electrodes, Co@NF-m exhibited the most favorable HER response, requiring an overpotential of only 61 mV to reach 10 mA cm^{-2}, which is substantially lower than those of NF-m (203 mV) and Co@NF (220 mV). The improved HER activity of Co@NF-m is also reflected in its lower Tafel slope of 76.6 mV dec^{-1} compared to those of the NF-m and Co@NF electrodes (Table 3), indicating faster HER kinetics.

Table 3. HER and OER kinetics parameters of the NF-m, Co@NF, and Co@NF-m electrodes.

Electrode	HER		OER	
	$\lvert\eta_{10}\rvert$ (mV)	Tafel Slope (mV dec^{-1})	$\lvert\eta_{10}\rvert$ (mV)	Tafel Slope (mV dec^{-1})
NF-m	203	86.9	420	100.9
Co@NF	220	118.8	304	91.4
Co@NF-m	61	76.6	241	92.5

A similar trend was observed for the OER activity, as shown in Figure 3c. Co@NF-m again demonstrated the best catalytic performance, reaching 10 mA cm^{-2} at an overpotential of 241 mV, whereas Co@NF and NF-m required 304 mV and 420 mV, respectively. The corresponding OER Tafel plots in Figure 3d show Tafel slopes of 92.5, 91.4, and 100.9 mV dec^{-1} for Co@NF-m, Co@NF, and NF-m, respectively. Although the OER Tafel slopes of Co@NF-m and Co@NF are relatively close, the markedly lower OER overpotential of Co@NF-m confirms its superior overall OER activity.

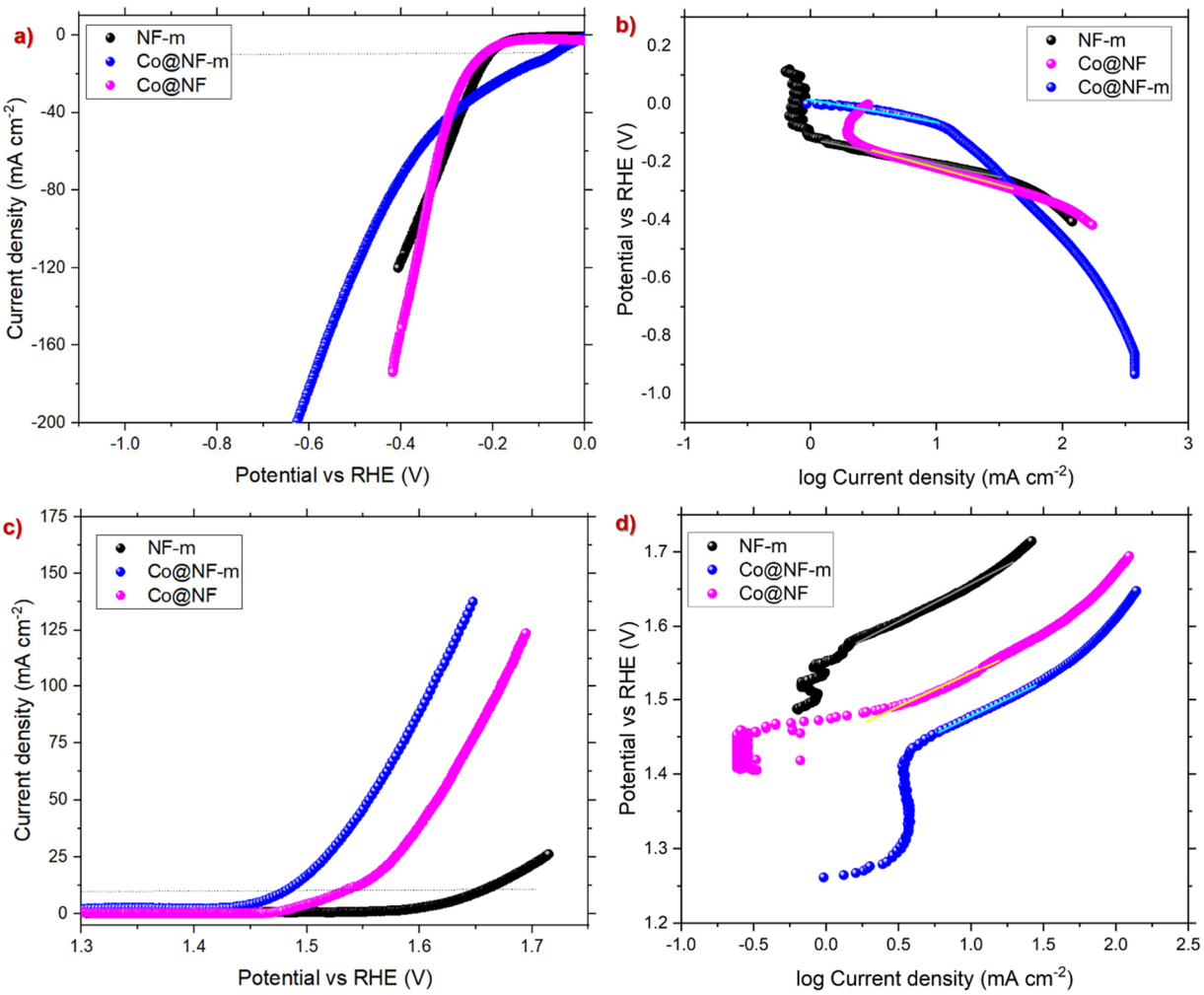

Figure 3. HER polarization curves of NF-m, Co@NF, and Co@NF-m in 1 M KOH (**a**), with the corresponding HER Tafel plots (**b**). OER polarization curves of NF-m, Co@NF, and Co@NF-m in 1 M KOH (**c**), with the corresponding OER Tafel plots (**d**). The current densities were normalized to the geometric areas of the electrodes.

The similar OER Tafel slopes of Co@NF and Co@NF-m suggest comparable apparent kinetic regimes, but they do not necessarily indicate identical electrochemically accessible active site populations or identical degrees of active-phase utilization. The Tafel slope describes the potential dependence of the reaction rate within the selected kinetic region, whereas the absolute overpotential also depends on the exchange current-related response, electrochemically accessible active-phase population, interfacial resistance, and electrode architecture. Consequently, similar slopes can coexist with horizontally shifted polarization curves and substantially different overpotential values at a fixed current density. Moreover, under anodic OER polarization, the initially deposited cobalt oxide/hydroxide surface may undergo partial electrochemical reconstruction to form more oxidized Co/Ni oxyhydroxide-like species. Therefore, the ex situ XPS and EDS results primarily describe the as-prepared electrodes, whereas the catalytically active surface under OER conditions may have evolved dynamically. The lower OER overpotential and higher baseline-subtracted cathodic redox charge of Co@NF-m are therefore interpreted as evidence of improved electrochemical accessibility and utilization of the redox-active phase, rather than as a direct measure of a static active-site density.

To place the bifunctional performance of Co@NF-m in the context of recent Ni/Co-based electrocatalysts, a comparison of the HER and OER metrics reported in alkaline media

is provided in Table S2. For additional benchmarking, representative literature values for commercial Pt/C toward the HER and commercial IrO_2/RuO_2 toward the OER, evaluated on nickel foam-based electrodes under comparable alkaline conditions, are also included. These noble-metal catalysts generally retain superior intrinsic activity, particularly for the HER, whereas Co@NF-m demonstrates competitive bifunctional performance using earth-abundant components and a scalable binder-free electrode architecture. Although direct comparison between different studies should be made cautiously because of differences in catalyst loading, electrode architecture, iR correction, and testing protocols, Co@NF-m exhibits competitive bifunctional activity, particularly in terms of its low HER overpotential and favorable OER overpotential at 10 mA cm^{-2}.

To further distinguish the contribution of the apparent electrochemical surface area to the intrinsic catalytic response, the HER and OER polarization curves were normalized using the corresponding C_{dl}-derived ECSA values. The ECSA-normalized HER curves are presented in Figure 4a. Despite exhibiting the lowest C_{dl}-derived ECSA among the Co-containing electrodes, Co@NF-m maintained the highest normalized HER current density over the investigated potential range. This behavior confirms that the superior HER performance of Co@NF-m is not caused by a larger capacitive surface area but rather by a more efficient electrochemical utilization of the active Co/Ni sites.

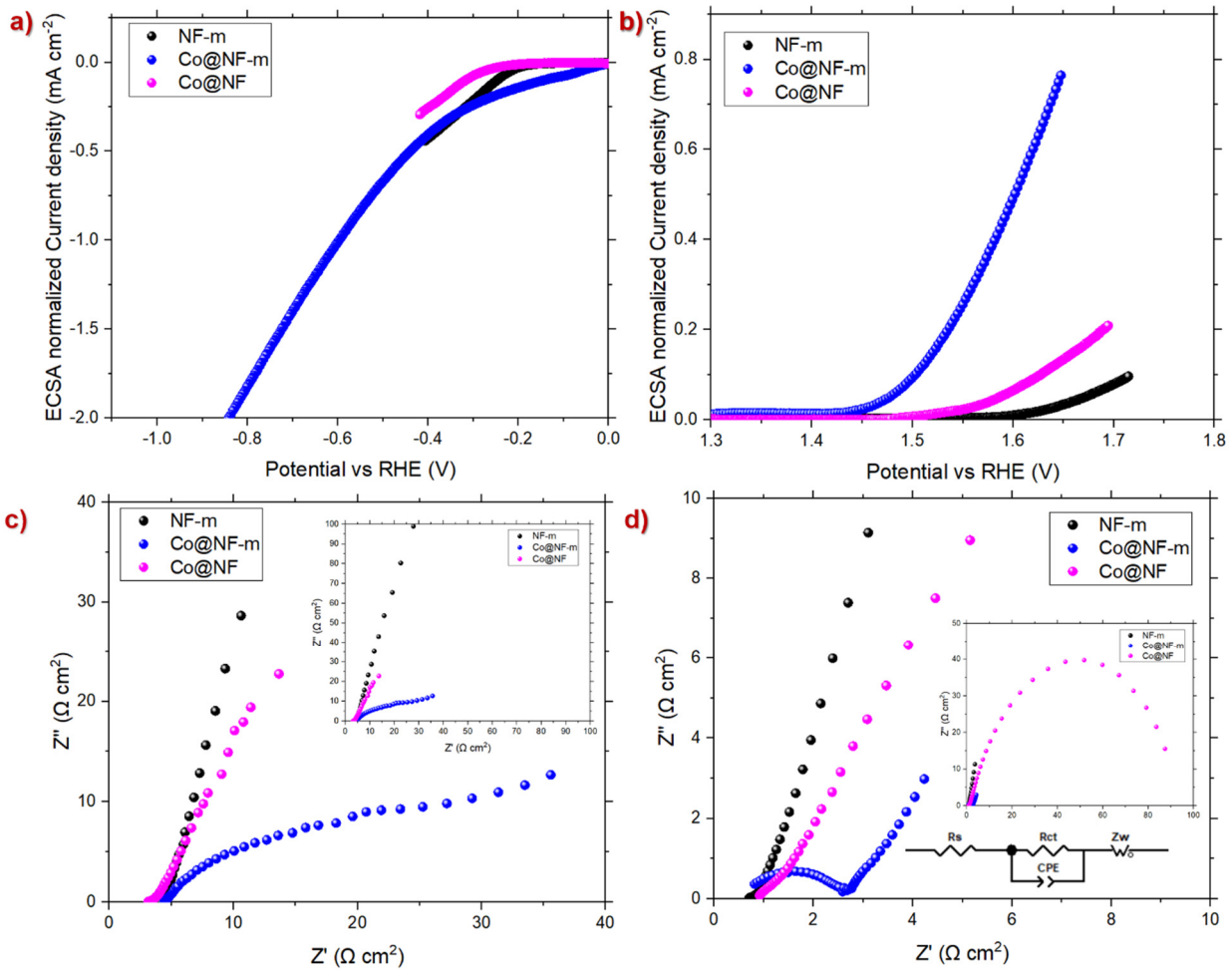

Figure 4. ECSA-normalized HER polarization curves (**a**) and ECSA-normalized OER polarization curves (**b**) for the NF-m, Co@NF, and Co@NF-m electrodes in 1 M KOH. Nyquist plots obtained under HER-relevant conditions (**c**) and OER-relevant conditions (**d**) are presented, with the inset illustrating the enlarged low-frequency/high-impedance region and the equivalent circuit employed for EIS fitting.

The same conclusion is supported by the ECSA-normalized OER polarization curves shown in Figure 4b. Co@NF-m again displayed the strongest normalized OER response, clearly outperforming both Co@NF and NF-m. This result is particularly important because Co@NF exhibits the highest C_{dl}-derived ECSA, whereas Co@NF-m exhibits the best ECSA-normalized activity. Therefore, the activity trend follows the integrated redox charge trend more closely than the C_{dl}-derived ECSA trend. This indicates that the higher bifunctional activity of Co@NF-m is associated with the increased participation of electrochemically accessible redox-active sites, as supported by the approximately 3.65-fold higher integrated redox charge discussed previously. SEM observations further indicated that the screen-printed Ni microparticle interlayer modified the surface architecture of the foam and influenced the morphology of the deposited Co-based phase. Together with the higher cathodic redox charge and more favorable apparent impedance response, these findings suggest that the interlayer enables more effective electrochemical accessibility and utilization of the deposited redox-active phase.

Electrochemical impedance spectroscopy was employed to further evaluate the interfacial electrochemical responses of the NF-m, Co@NF, and Co@NF-m electrodes under HER- and OER-relevant conditions. The corresponding Nyquist plots are shown in Figure 4c,d, and the fitted parameters are listed in Table 4.

Table 4. EIS fitting parameters of NF-m, Co@NF, and Co@NF-m measured at 1.5 V vs. RHE for OER and −0.3 V vs. RHE for HER. The fitted R_{ct} values were treated as apparent charge-transfer resistances owing to the porous electrode architecture and distributed capacitive/transport contributions.

Electrode	Condition	R_s Ω cm^2	R_{ct} Ω cm^2	CPE-T Fs^{n-1}cm^{-2}	CPE-P, n	W Ω s$^{-1/2}$
NF-m	HER	3.96	1113	0.01075	0.946	11.04
Co@NF	HER	3.25	46.24	0.283	0.98	3.66
Co@NF-m	HER	4.04	41.25	0.018	0.51	2.62
NF-m	OER	0.74	79.6	0.168	0.98	2.05
Co@NF	OER	1.65	93.25	0.004	0.88	-
Co@NF-m	OER	0.69	1.67	0.0002	0.865	2.59

Under HER conditions, NF-m exhibited a substantially larger apparent R_{ct}, indicating sluggish interfacial charge transfer in the absence of the Co-based active phase. After cobalt deposition, both Co-containing electrodes showed a pronounced decrease in the apparent R_{ct}, with Co@NF-m displaying the lowest value among the HER-tested electrodes. The relatively close R_{ct} values of Co@NF and Co@NF-m indicate that the markedly superior HER polarization response of Co@NF-m cannot be explained by the charge-transfer resistance alone. Instead, the impedance results should be considered together with the higher redox charge, ECSA-normalized activity, and modified surface architecture, which collectively indicate more effective electrochemical utilization of the Co/Ni redox-active phase. The relatively low CPE exponent of Co@NF-m indicates a more distributed and non-ideal capacitive response, which is expected for a hierarchical porous electrode architecture. This behavior is consistent with a heterogeneous interface containing a broad distribution of local time constants, rather than with inherently inferior catalytic performance.

Under OER-relevant conditions, Co@NF-m also exhibited the most favorable impedance response, with a markedly lower apparent R_{ct} than both NF-m and Co@NF. This behavior agrees well with the lower OER overpotential and the enhanced ECSA-normalized OER activity. The fact that Co@NF exhibited a somewhat higher apparent R_{ct} than NF-m at the selected OER bias, despite showing better polarization performance, further demonstrates that a single fitted impedance parameter cannot independently describe the overall electrocatalytic response. Differences in redox state evolution, surface

reconstruction, accessible active-phase population, and distributed transport processes can also affect the impedance spectrum. The inclusion of Warburg-type contributions in most fits further suggests that ion transport and diffusion-related processes contribute to the overall impedance response of porous electrodes.

Overall, the ECSA-normalized polarization curves and EIS analysis indicate that the enhanced bifunctional activity of Co@NF-m cannot be explained by its apparent capacitive surface area. Instead, the improved HER/OER performance is mainly associated with higher redox-active site participation, favorable interfacial electrochemical behavior, and effective integration of the Co-based active layer within the screen-printed NF-m architecture.

The long-term operational stability of the electrodes was further evaluated under constant current conditions in 1 M KOH solution. As shown in Figure 5a, during the HER operation at -100 mA cm^{-2}, Co@NF-m maintained the lowest overpotential throughout the test, indicating a more favorable hydrogen evolution performance under prolonged cathodic polarization. In comparison, Co@NF required a slightly more negative potential, whereas NF-m exhibited the largest cathodic potential, consistent with its inferior HER activity observed in polarization and Tafel analyses. The nearly stable potential profile of Co@NF-m over the entire testing period demonstrates its good durability under demanding HER conditions.

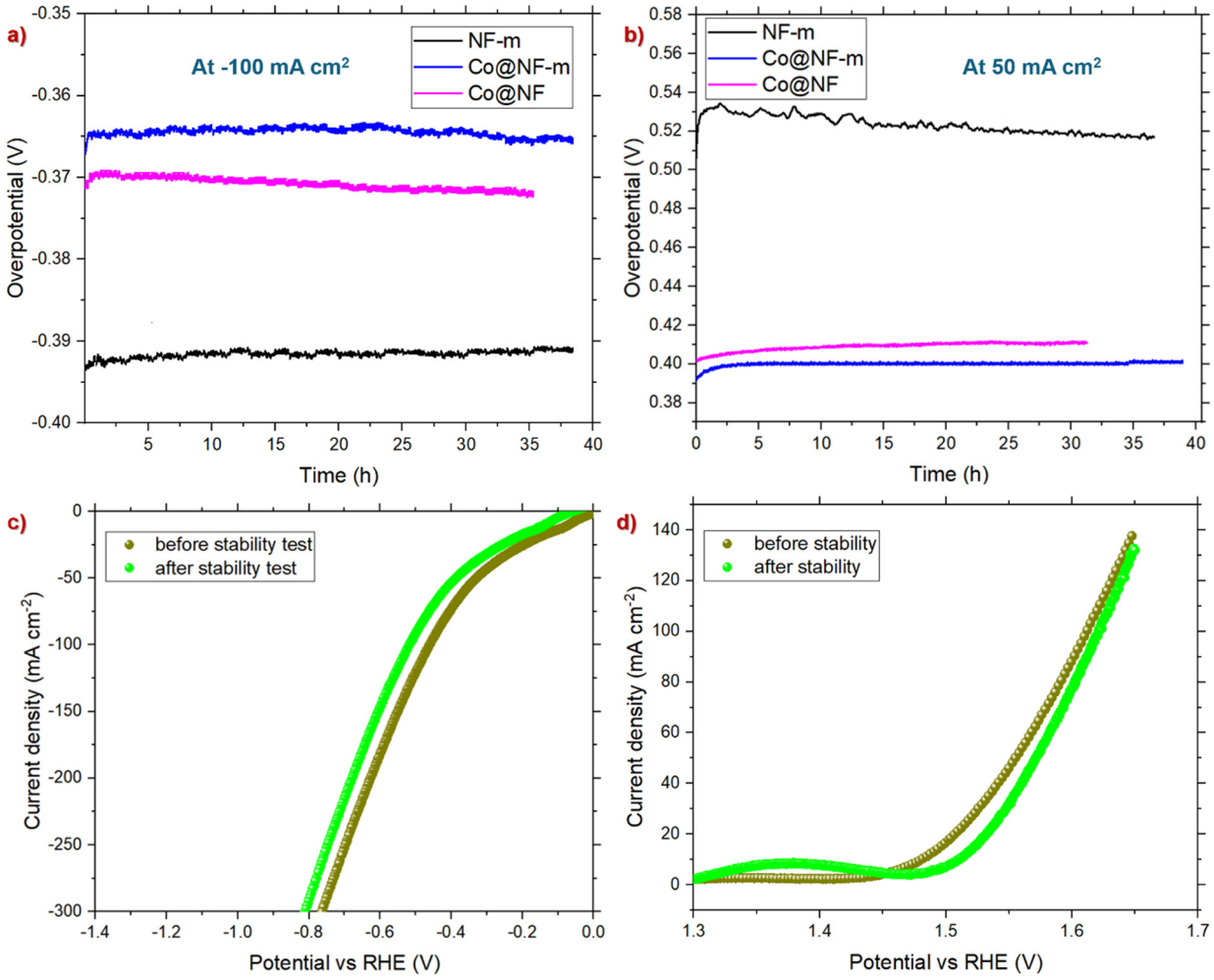

Figure 5. Chronopotentiometric stability tests of the NF-m, Co@NF, and Co@NF-m electrodes under HER operation at -100 mA cm^{-2} (**a**) and OER operation at 50 mA cm^{-2} (**b**) in 1 M KOH solution. HER polarization curves of Co@NF-m before and after the stability test (**c**). OER polarization curves of Co@NF-m before and after the stability test (**d**). The current densities were normalized to the geometric electrode area.

A similar stability trend was observed during the OER at 50 mA cm^{-2}, as shown in Figure 5b. Co@NF-m displayed the lowest and most stable anodic potential among the tested electrodes, whereas NF-m required a considerably higher potential and exhibited more pronounced fluctuations in potential during anodic polarization. This behavior confirms the limited OER activity of the modified substrate in the absence of the Co-based active phase during OER. In addition, the less stable response of NF-m may be partly associated with the fact that this substrate consists of an ambient-dried screen-printed Ni/polymer interlayer without the subsequent solvothermal deposition and calcination treatment applied during the fabrication of Co@NF-m. In contrast, the solvothermal growth of the Co-based phase, followed by thermal treatment, is expected to promote stronger structural integration of the Ni microparticle interlayer and the active cobalt oxide/hydroxide phase, thereby contributing to the more stable OER response of Co@NF-m.

To further assess the durability of Co@NF-m after prolonged operation, polarization curves were recorded before and after the stability tests. For HER (Figure 5c), the post-stability polarization curve showed only a moderate shift relative to the initial response, indicating that the electrode largely preserved its cathodic activity after operation at -100 mA cm^{-2}. Similarly, the OER polarization curves before and after the stability testing (Figure 5d) remained comparable, with only a slight decrease in the current density after prolonged anodic polarization. This minor activity loss may be associated with surface reconstruction, partial blocking of active sites, or gas bubble-related effects during long-term operation.

Post-stability SEM analysis of Co@NF-m (Figure S6) further supports the electrochemical durability results. The electrode retained a rough and porous surface morphology after the stability test, without evidence of severe structural collapse or large-scale delamination of the Co-based active layer. Although local surface rearrangement after prolonged HER/OER operation cannot be excluded, the preservation of the hierarchical texture indicates good mechanical integration between the solvothermal-grown Co-based phase and screen-printed NF-m interlayer. The retention of the rough, porous morphology after durability testing suggests that the screen-printed interlayer helps preserve both the adhesion and the hierarchical architecture of the active Co-based phase. This morphological robustness is consistent with the stable chronopotentiometric profiles and retained polarization response after durability testing.

In addition, the zero-gap bifunctional two-electrode water-splitting performance was evaluated using the optimized electrode configuration separated by a Zirfon Perl 500 diaphragm in a 6 M KOH solution at room temperature (Figure 6). In this configuration, the anode (Co@NF-m) and cathode (Co@NF-m) were pressed against the separator to minimize the interelectrode distance and reduce the ohmic losses, while maintaining physical separation between the evolved gases. Chronopotentiometric measurements were performed under galvanostatic conditions, and the recorded values were reported as the absolute cell voltages. The assembled zero-gap electrolyzer rapidly reached a stable operating voltage after the initial activation period, indicating efficient ionic transport through the Zirfon separator and good electrical contact within the cell. At a current density of 200 mA cm^{-2} for 25 h, the cell maintained a low and nearly steady voltage, demonstrating the suitability of the Co-based NF electrodes for practical alkaline water-splitting operations under intensified conditions. The zero-gap electrolyzer required approximately 1.87 V at 200 mA cm^{-2}, suggesting a promising high-current two-electrode alkaline water-splitting performance under intensified testing conditions.

Overall, the combined electrochemical evidence suggests that the superior bifunctional response of Co@NF-m is not controlled by a single performance descriptor, such as the apparent capacitive surface area. Rather, the activity enhancement results from

the interplay between electrochemically accessible Co/Ni redox-active sites, efficient integration of the cobalt-based phase with the screen-printed Ni microparticle interlayer, and favorable interfacial electrochemical behavior within the hierarchical porous structure. This interpretation is further supported by the ECSA-normalized polarization response, which decouples the activity trend from the C_{dl}-derived ECSA, and by the impedance analysis, which indicates improved apparent charge transfer characteristics while retaining a distributed porous electrode behavior. The stable chronopotentiometric response and preserved post-operative morphology further confirm that the engineered Co@NF-m architecture combines high activity with structural robustness. Thus, the role of the screen-printed interlayer extends beyond simple roughness enhancement, acting as an integrated conductive and mechanically stable platform that improves the utilization and durability of the Co-based active phase.

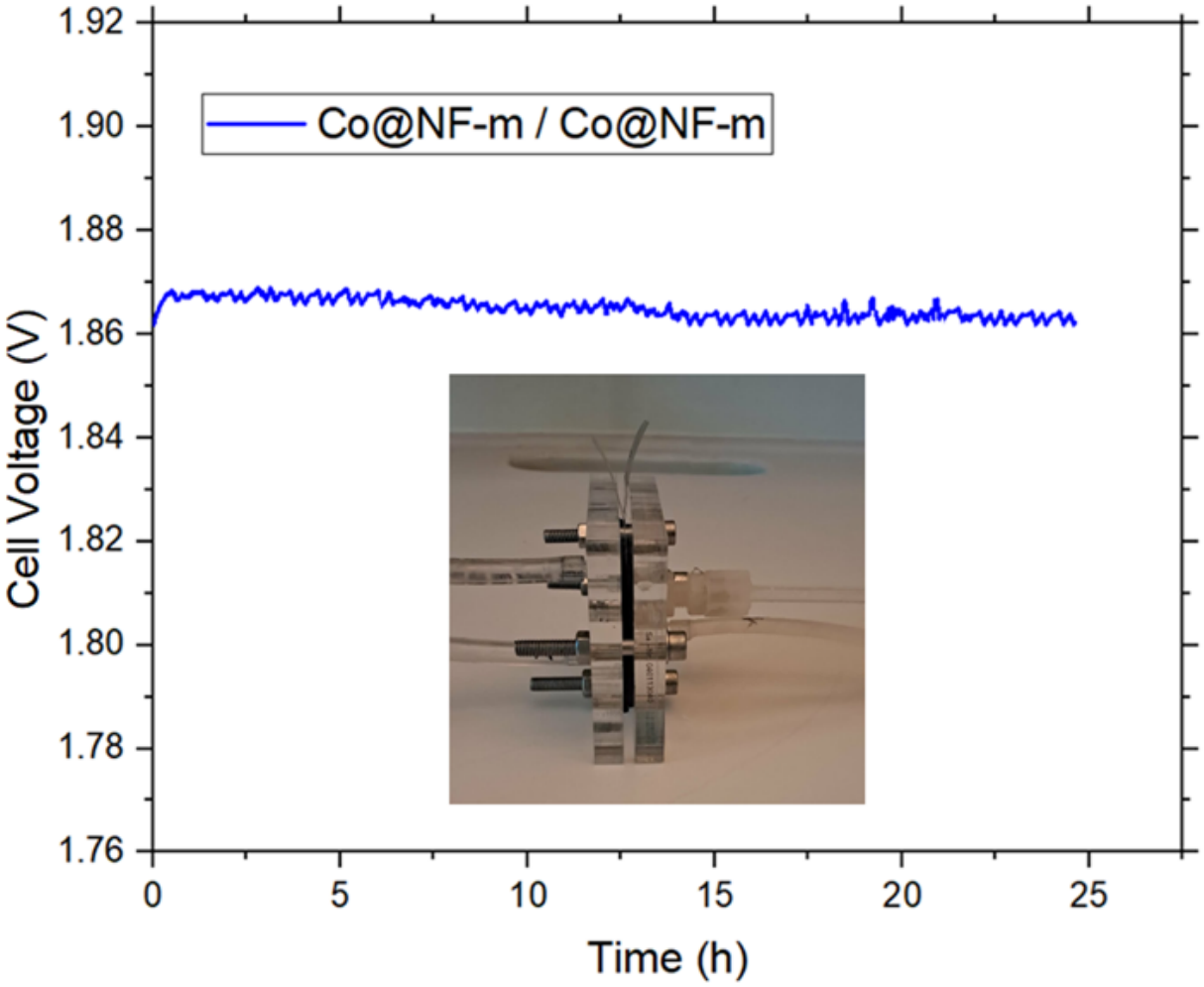

Figure 6. Chronopotentiometric response of the zero-gap two-electrode alkaline electrolyzer using a Zirfon Perl 500 separator (Agfa) at 200 mA cm^{-2} in 6 M KOH solution.

From a manufacturing perspective, the proposed approach is attractive because screen printing is compatible with patterned and large-area deposition, straightforward control of the coating thickness and loading, and the use of commercial porous metal substrates. The printed Ni microparticle/polymer interlayer can be produced using relatively simple and scalable equipment and subsequently acts as a structured scaffold for solvothermal Co growth. In principle, the solvothermal step may also be adapted to larger substrates through scaled batch reactors or continuous processing. Nevertheless, practical scale-up re-

quires careful control of ink rheology, coating uniformity, precursor transport, temperature distribution, reproducibility, and process energy demand.

3. Experimental Section

3.1. Materials

All materials used in this study were employed as received without additional purification. These materials include potassium hydroxide (KOH, technical grade, Sigma-Aldrich, Heraklion, Greece), ethanol (CH_3CH_2OH, 99.8%, ACROS Organics, Geel, Belgium), hydrochloric acid (HCl, 37%, Sigma Aldrich, Tokyo, Japan), cobalt(II) nitrate hexahydrate ($Co(NO_3)_2 \cdot 6H_2O$, 98%, Sigma Aldrich, Tokyo, Japan), nickel foam (99.8%, Changzhou DLX Alloy Co., Changzhou, China, 90% porosity, 90 ppi), nickel powder (Vale Type 255, 99.9%, Fisher, sub-sieve size 2.2–2.6 μm), Zirfon Perl 500 (Agfa Corporate, Germany, Düsseldorf), polyvinyl alcohol (PVA, Sigma Aldrich, Tokyo, Japan), polyacrylic acid (PAA, Sigma Aldrich, Tokyo, Japan), and polyethylene glycol (PEG, Sigma Aldrich, Tokyo, Japan).

3.2. Fabrication of the Modified Ni Foam Substrate

To improve the growth and adhesion of cobalt nanostructures, a nickel foam substrate was modified by incorporating a porous nickel microparticle interlayer via screen printing, as described in our previous study [18]. Briefly, the ink formulation commenced by dissolving polyvinyl alcohol and polyacrylic acid in deionized water to establish a binder–dispersant system. The solution was gently heated to approximately 70 °C to ensure complete polymer dissolution and subsequently cooled to room temperature. Polyethylene glycol (PEG) was added as a viscosity modifier and plasticizer to improve the printability and flexibility of the deposited layers. High-purity Ni powder was gradually incorporated into the prepared binder solution under continuous mechanical stirring. The resulting slurry was mixed under vacuum at 250 rpm for 2 h to eliminate trapped air and ensure compositional homogeneity, and was subsequently deposited onto the nickel foam through a screen-printing process to form a thin Ni-255/polymer interlayer on the nickel foam. The printed substrates were dried at room temperature for 24 h, yielding modified nickel foam substrates for the subsequent deposition of cobalt. The gravimetrically determined loading of the screen-printed Ni microparticle/polymer interlayer was 12 mg cm^{-2}.

Notably, the NF-m substrate maintained sufficient structural and mechanical integrity after drying at ambient temperature, without requiring a conventional thermal sintering step. The hydrophilic PVA/PAA/PEG binder system not only provided strong adhesion between the nickel particles and nickel foam but also promoted electrolyte wettability and accessibility of the porous network. Consequently, the modified substrate offered an enlarged accessible surface area, favoring the subsequent homogeneous growth of cobalt nanostructures.

3.3. Solvothermal Fabrication of Co@NF and Co@NF-m

The solvothermal fabrication of Co_xOy electrodes on commercial NF and NF-m was described in our previous studies [8,28]. In summary, 16 mmol of $Co(NO_3)_2 \cdot 6H_2O$ was dissolved in 40 mL of pure ethanol. The NF or NF-m substrates, together with this solution, were enclosed in a stainless-steel autoclave lined with Teflon and heated for 10 h at 120 °C. Following this, the Co@NF and Co@NF-m electrodes were repeatedly washed using deionized water and ethanol, then left to dry at 60 °C for a duration of 12 h, and then calcined in air at 300 °C for 3 h with a heating rate of 5 °C/min. The use of 16 mmol of the Co precursor was determined based on prior studies, which demonstrated that this quantity represented optimal loading [29,30]. The gravimetrically determined cobalt loadings were 6.10 ± 0.20 mg cm^{-2} for Co@NF and 5.87 ± 0.25 mg cm^{-2} for Co@NF-m, reported as

mean ± standard deviation from three independently prepared electrodes. This loading was determined gravimetrically by weighing the nickel foam substrate before and after the solvothermal growth on an analytical balance.

Crucially, the subsequent solvothermal deposition of cobalt served a dual purpose: it drove the uniform growth of active cobalt nanostructures and simultaneously triggered in situ thermal esterification and cross-linking of the ambient-dried PVA/PAA polymer matrix [31]. The solvothermal environment transforms the water-soluble binder into an insoluble, chemically robust, and highly hydrophilic polymeric network [32]. This in situ engineering approach successfully locks the screen-printed nickel microparticles to the nickel foam substrate, guaranteeing excellent mechanical durability during long-term stability testing while maintaining the open porosity required for a high-rate hydrogen evolution reaction.

3.4. Physicochemical Characterization

The crystalline structure, surface morphology, elemental composition, porous characteristics, and surface chemical states of the fabricated electrodes were systematically investigated using complementary physicochemical characterization techniques. The phase composition and crystallographic properties of the samples were examined by X-ray diffraction (XRD) using a Rigaku MiniFlex II diffractometer with Cu Kα radiation (λ = 1.5406 Å), operated at 30 kV and 15 mA.

The electrodes' surface morphology and microstructural characteristics were examined using field-emission scanning electron microscopy (FE-SEM, Zeiss Crossbeam 350) across a range of magnifications. Energy-dispersive X-ray spectroscopy (EDS), combined with the SEM system, was used to evaluate the elemental composition and distribution. To delve deeper into the surface chemical composition and oxidation states of the elements, X-ray photoelectron spectroscopy (XPS) was conducted with a SPECS FlexMod spectrometer, featuring a monochromated Al Ka X-ray source (hν = 1486.6 eV). Both survey and high-resolution core-level spectra were obtained at pass energies of 100 eV and 20 eV, respectively. Calibration of all spectra was achieved by aligning the adventitious carbon C 1s peak to a binding energy of 284.8 eV.

3.5. Electrochemical Measurements

The electrocatalytic performance of the fabricated electrodes for the hydrogen evolution reaction (HER) and oxygen evolution reaction (OER) was systematically evaluated using cyclic voltammetry (CV), linear sweep voltammetry (LSV), staircase voltammetry (SCV), electrochemical impedance spectroscopy (EIS), long-term stability measurements, and a zero-gap two-electrode setup. To assess the reproducibility of the fabrication procedure, three independently prepared electrodes of each type were tested under identical experimental conditions.

Electrochemical measurements were conducted at room temperature (25 °C) utilizing a VersaSTAT 4 potentiostat/galvanostat, arranged in a standard three-electrode setup. The prepared electrodes served as the working electrodes, while a graphite rod and Ag/AgCl electrode (3.5 M KCl) were employed as the counter and reference electrodes, respectively. The exposed geometric area of each working electrode was 1.0 cm^2, and all geometric current densities reported throughout the manuscript were calculated using this projected electrode area. Three-electrode HER/OER measurements were performed in 1 M KOH, whereas the zero-gap two-electrode electrolyzer was evaluated in a 6 M KOH solution. Prior to each experiment, the electrolyte was purged with high-purity nitrogen (99.999%) for at least 15 min to remove dissolved oxygen and establish stable electrochemical conditions in the cell. All measurements were repeated at least three times using independently fabricated

electrodes to verify experimental reproducibility. The potentials measured versus Ag/AgCl were converted to the reversible hydrogen electrode (RHE) scale according to the Nernst Equation (2):

$$E_{RHE} = E_{Ag/AgCl} + 0.059\,pH + E^0_{Ag/AgCl} \quad (2)$$

where $E^0_{Ag/AgCl}$ is the standard potential of the Ag/AgCl reference electrode, and the pH of 1 M KOH was taken as 13.6.

For HER polarization measurements, LSV was performed using 95% real-time dynamic iR compensation applied by the potentiostat. The uncompensated resistance, R_u, was determined separately for each electrode immediately before the polarization measurement from the high-frequency impedance response. Accordingly, the instrument corrected 95% of the instantaneous iR_u drop during data acquisition, while no additional post-measurement correction was applied.

OER polarization curves were obtained by staircase voltammetry in 1 M KOH by stepping the potential anodically from 1.0 to 1.8 V vs. RHE. OER measurements were also performed using 95% real-time dynamic iR compensation. No additional post-processing iR correction was applied.

The HER Tafel slopes were obtained by linear regression of the quasi-linear regions of the η versus log j plots. The fitting regions encompassed the benchmark current density of 10 mA cm^{-2}, corresponding approximately to current-density ranges of 1–25, 3–35, and 1–15 mA cm^2 for NF-m, Co@NF, and Co@NF-m, respectively. For the OER, the Tafel slopes were determined from the quasi-linear regions above the main Co/Ni surface-redox features, where oxygen evolution dominated the Faradaic response. The approximate fitting potential ranges were 1.58–1.69, 1.47–1.55, and 1.45–1.52 V vs. RHE for NF-m, Co@NF, and Co@NF-m, respectively.

Cyclic voltammetry measurements were conducted in 1 M KOH within the potential range of 1.0 to1.6 V versus RHE. The electrochemically active surface area (ECSA) was estimated using the double-layer capacitance (C_{dl}) values derived from cyclic voltammetry (CV) measurements conducted within non-Faradaic potential windows: 0.37–0.52 V vs. RHE for NF-m, 0.72–0.87 V vs. RHE for Co@NF, and 0.40–0.52 V vs. RHE for Co@NF-m. These measurements were performed at scan rates ranging from 5 to 100 mV s^{-1}.

Electrochemical impedance spectroscopy measurements were carried out at a DC bias potential of 1.5 V (for OER) and −0.3 V (for HER) versus RHE using AC perturbation amplitudes of 5 and 10 mV over a frequency range of 10 mHz to 10 kHz. ZView software v.3.4e was employed to analyze the impedance spectra, which were then modeled using an equivalent circuit. This circuit included the solution resistance (R_s) in series, paired with a parallel arrangement of the charge-transfer resistance (R_{ct}) and a constant phase element (CPE). The CPE parameters (CPE-T and CPE-P) were used to describe the deviations from the ideal capacitive behavior, which is associated with surface heterogeneity and interfacial effects. All impedance spectra were initially fitted using the same base equivalent circuit, consisting of the solution resistance in series with a parallel R_{ct}—CPE element. A Warburg element was included only when the experimental spectrum exhibited a distinct low-frequency diffusion-related tail and when its inclusion provided a meaningful improvement in the fitting quality and residual distribution. For spectra without a clear diffusion-related contribution, the Warburg element was omitted to avoid overparameterization. Owing to the hierarchical porous electrode architecture and the possible overlap between the charge transfer, capacitive, and mass transport processes, the fitted R_{ct} values were treated as apparent interfacial descriptors rather than absolute kinetic constants. The long-term operational stability of the electrodes was evaluated using chronopotentiometric measurements at constant current densities of 100 mA cm^{-2} (for HER) and 50 mA cm^{-2} (for OER) for approximately 40 h in a 1 M KOH solution. The electrode potential was

continuously monitored throughout the test to assess the durability of the catalysts under prolonged operating conditions. For the 2-electrode setup, a custom-made cell was used along with a Zirfon Perl 500 membrane for gas separation.

4. Conclusions

This study introduces a screen-printed nickel microparticle/interlayer positioned between commercial nickel foam and a solvothermally grown cobalt-based oxide/hydroxide phase. The objective of this study was to examine the impact of substrate engineering on bifunctional hydrogen evolution reaction (HER) and oxygen evolution reaction (OER) electrocatalysis. The principal scientific finding was that the electrocatalytic activity was not governed by the C_{dl}-derived apparent surface area alone. Although Co@NF exhibited the highest apparent ECSA, the screen-printed Co@NF-m delivered the lowest HER and OER overpotentials, the strongest ECSA-normalized responses, and an approximately 3.65-fold higher baseline-subtracted cathodic redox charge than that of Co@NF.

These results indicate that the screen-printed interlayer alters the growth environment, morphology, and structural integration of the Co-based phase, thereby promoting more effective electrochemical accessibility and utilization of the redox-active material. The impedance results further suggest a more favorable apparent interfacial response, while the retained porous morphology and stable chronopotentiometric behavior demonstrate that the interlayer contributes to the mechanical robustness of the electrode architecture.

Thus, the fundamental contribution of this study is the demonstration that an intermediate conductive microparticle layer can decouple the catalytic performance from the apparent capacitive surface area by controlling the active-phase utilization, interfacial electrochemical behavior, and structural stability. This establishes screen-printed interlayer engineering as a general design strategy for optimizing porous, binder-integrated, and bifunctional electrodes for alkaline water electrolysis.

Supplementary Materials: The following supporting information can be downloaded at: https://www.mdpi.com/article/10.3390/catal16080665/s1, Figure S1: High-resolution Ni 2p XPS spectra of NF-m, Co@NF-m, and Co@NF, showing the characteristic Ni^{2+} $2p_{3/2}$ and $2p_{1/2}$ components together with their satellite peaks; Figure S2: High-resolution Co 2p XPS spectra of Co@NF and Co@NF-m, showing Co $2p_{3/2}$ and Co $2p_{1/2}$ components with characteristic satellite features; Figure S3: High-resolution O 1s XPS spectra of NF-m, Co@NF-m, and Co@NF, deconvoluted into metal-oxygen (M-O), surface hydroxyl (M-OH), and adsorbed H_2O/oxygenated species contributions [18]; Figure S4: CV measurements recorded in a non-faradaic potential region at different scan rates to calculate C_{DL} values of the NF-m, Co@NF-m and Co@NF electrodes; Figure S5: Cathodic CV branches of NF-m, Co@NF, and Co@NF-m recorded at 10 mV s^{-1} within the common integration window of 1.00–1.40 V vs. RHE. The straight lines represent the local linear baselines; Figure S6: SEM images of the Co@NF-m electrode after OER and HER stability tests; Table S1: Crystallite size estimation for Co@NF-m from selected XRD reflections using the Scherrer equation. The contribution near 44.5–44.8° should be interpreted with caution because of overlap between the metallic Ni substrate reflection and possible Co-containing contributions; Table S2: Comparison of the HER and OER performance of Co@NF-m with recently reported Ni/Co-based bifunctional electrocatalysts in alkaline electrolyte; Table S3: Baseline-subtracted cathodic redox charges obtained from CV profiles recorded at 10 mV s^{-1} within a common potential window of 1.00–1.40 V vs. RHE [33–44].

Author Contributions: Conceptualization, I.P. and M.K. (Michalis Konsolakis); methodology, I.P., B.K., M.A., M.K. (Michalis Konsolakis), S.P. and J.M.; investigation, I.P., B.K., M.A., M.K. (Michalis Konsolakis) and S.P.; data curation, I.P.; formal analysis, I.P., B.K. and M.K. (Majewska Karolina); writing—original draft preparation, I.P.; writing—review and editing, all authors; visualization, I.P.; supervision, J.M. and M.K. (Michalis Konsolakis); project administration, M.K. (Michalis Konsolakis). All authors have read and agreed to the published version of the manuscript.

Funding: This research was partially funded by the Warsaw University of Technology within the Excellence Initiative: Research University (IDUB) program (agreement nr CPR-IDUB/370/Z01/2023).

Institutional Review Board Statement: Not applicable.

Informed Consent Statement: Not applicable.

Data Availability Statement: The data supporting the findings of this study are available within the article and the Supplementary Materials. Additional raw data are available from the corresponding author upon reasonable request.

Acknowledgments: The authors would like to thank Mateusz Włoczewski (Institute of Fundamental Technological Research of the Polish Academy of Sciences) for his assistance with the XRD analysis and Evangelia Skliri (IESL-FORTH, Greece) for the XPS analysis.

Conflicts of Interest: The authors declare no conflicts of interest.

References

1. Zhang, R.; Zhang, S.; Zhang, J. Polymer Electrolyte Membrane Water Electrolysis for Hydrogen Energy: Advanced Electrocatalysts, Membranes, and Functional Mechanisms. *Electrochem. Energy Rev.* **2026**, *9*, 14. [CrossRef]
2. Rao, X.; Zhang, S.; Zhang, J. Carbon Semi-Tubes for Electrochemical Energy Catalysis. *Electrochem. Energy Rev.* **2025**, *8*, 7. [CrossRef]
3. Poimenidis, I.; Papakosta, N.; Loukakos, P.A.; Marnellos, G.E.; Konsolakis, M. Highly Efficient Cobalt Sulfide Heterostructures Fabricated on Nickel Foam Electrodes for Oxygen Evolution Reaction in Alkaline Water Electrolysis Cells. *Surfaces* **2023**, *6*, 493–508. [CrossRef]
4. Song, R.; Wang, X.; Ge, J. Recent progress of noble metal-based single-atom electrocatalysts for acidic oxygen evolution reaction. *Curr. Opin. Electrochem.* **2023**, *42*, 101379. [CrossRef]
5. Poimenidis, I.; Skliri, E.; Kourmouli, E.; Binas, V.; Konsolakis, M. Tailoring nickel foam-based electrocatalysts via oxidation-reduction pretreatment and Ni deposition for enhanced oxygen evolution reaction in alkaline media. *J. Power Sources* **2026**, *676*, 239802. [CrossRef]
6. Zhang, W.; Han, N.; Dou, Y.; Zhang, X.; Luo, J.; Dou, S.; Fransaer, J. Applications of Cobalt Phosphide-Based Materials in Electrocatalysis. *ACS Catal.* **2025**, *15*, 5457–5479. [CrossRef]
7. Xu, K.; Liang, X.; Ge, X.; Liu, W.; Zhang, S.; Liu, J. Recent progress in cobalt-based non-noble-metal electrocatalysts for acidic oxygen evolution reaction: A review. *Curr. Opin. Electrochem.* **2026**, *56*, 101817. [CrossRef]
8. Poimenidis, I.A.; Lykaki, M.; Loukakos, P.A.; Konsolakis, M. Ultra-high supercapacitor performance of NiSRu@NiO nanocomposites on nickel foam electrodes. *J. Energy Storage* **2024**, *83*, 110679. [CrossRef]
9. Hu, Y.; Hu, C.; Du, A.; Xiao, T.; Yu, L.; Yang, C.; Xie, W. Interfacial Evolution on Co-based Oxygen Evolution Reaction Electrocatalysts Probed by Using In Situ Surface-Enhanced Raman Spectroscopy. *Anal. Chem.* **2022**, *95*, 1703–1709. [CrossRef] [PubMed]
10. Liang, Z.; Shen, D.; Wang, L.; Fu, H. Recent progress of cobalt-based electrocatalysts for water splitting: Electron modulation, surface reconstitution, and applications. *Nano Res.* **2024**, *17*, 2234–2269. [CrossRef]
11. Poimenidis, I.A.; Papakosta, N.; Klini, A.; Farsari, M.; Konsolakis, M.; Loukakos, P.A.; Moustaizis, S.D. Electrodeposited Ni foam electrodes for increased hydrogen production in alkaline electrolysis. *Fuel* **2023**, *342*, 127798. [CrossRef]
12. Poimenidis, I.A.; Liapakis, M.; Klini, A.; Farsari, M.; Moustaizis, S.D.; Loukakos, P.A.; Konsolakis, M. Ni deposition on nickel foam via the use of high-frequency currents for enhanced hydrogen evolution reaction in alkaline media. *J. Phys. Chem. Solids* **2025**, *207*, 112930. [CrossRef]
13. Ratsoma, M.S.; Poho, B.L.O.; Makgopa, K.; Raju, K.; Modibane, K.D.; Jafta, C.J.; Oyedotun, K.O. Application of Nickel Foam in Electrochemical Systems: A Review. *J. Electron. Mater.* **2023**, *52*, 2264–2291. [CrossRef]
14. Poimenidis, I.; Konsolakis, M. Monometallic nickel as a tunable electrocatalyst for alkaline hydrogen evolution: A critical review. *J. Mater. Chem. A* **2026**, *14*, 16332–16360. [CrossRef]
15. Jiang, W.; Li, H.; Yang, X.; Chen, Y.; Eckert, K. Magnetic field-assisted jet electrodeposition of Ni–Co based composite electrodes on nickel foam for alkaline water electrolysis. *Int. J. Hydrogen Energy* **2026**, *197*, 152636. [CrossRef]
16. Yhobu, Z.; Sreeramareddygari, M.; Phanthong, C.; Budagumpi, S.; Nagaraju, D.H.; Chaiworn, W.; Somasundrum, M.; Rijiravanich, P.; Chuangchote, S.; Surareungchai, W. Gel-derived NiO–MoS_2 for the scalable fabrication of bifunctional screen-printed electrodes for overall water splitting. *Int. J. Hydrogen Energy* **2025**, *139*, 247–256. [CrossRef]
17. Hughes, J.P.; Blanco, F.D.; Banks, C.E.; Rowley-Neale, S.J. Mass-producible 2D-WS2 bulk modified screen printed electrodes towards the hydrogen evolution reaction. *RSC Adv.* **2019**, *9*, 25003–25011. [CrossRef] [PubMed]

18. Poimenidis, I.; Bochenek, K.; Martsinchyk, A.; Majewska, K.; Shuhayeu, P.; Milewski, J.; Konsolakis, M. High-performance supercapacitor based on cobalt nanostructures directly grown on engineered nickel foam substrate with enhanced ion transport and cycling stability. *Next Mater.* **2026**, *12*, 102264. [CrossRef]
19. Bhatti, A.L.; Tahira, A.; Gradone, A.; Mazzaro, R.; Morandi, V.; Aftab, U.; Abro, M.I.; Nafady, A.; Qi, K.; Infantes-Molina, A.; et al. Nanostructured Co_3O_4 electrocatalyst for OER: The role of organic polyelectrolytes as soft templates. *Electrochim. Acta* **2021**, *398*, 139338. [CrossRef]
20. Wagh, K.S.; Mane, S.M.; Teli, A.M.; Shin, J.C.; Lee, J. Recent Advancements in Co_3O_4-Based Composites for Enhanced Electrocatalytic Water Splitting. *Micromachines* **2024**, *15*, 1450. [CrossRef] [PubMed]
21. Johnson, E.; Prasannakumar, A.T.; Chandran, S.R.; Krishnan, R.R.; Nisha, S.K.; Prema, K. Co_3O_4 nanoflower anchored CuO nanostructure as efficient electrocatalyst for oxygen evolution reaction. *Inorg. Chem. Commun.* **2026**, *183*, 115847. [CrossRef]
22. Lykhach, Y.; Piccinin, S.; Skála, T.; Bertram, M.; Tsud, N.; Brummel, O.; Camellone, M.F.; Beranová, K.; Neitzel, A.; Fabris, S.; et al. Quantitative Analysis of the Oxidation State of Cobalt Oxides by Resonant Photoemission Spectroscopy. *J. Phys. Chem. Lett.* **2019**, *10*, 6129–6136. [CrossRef] [PubMed]
23. Zhang, Y.; Gao, L.; Hensen, E.J.M.; Hofmann, J.P. Evaluating the Stability of Co_2 P Electrocatalysts in the Hydrogen Evolution Reaction for Both Acidic and Alkaline Electrolytes. *ACS Energy Lett.* **2018**, *3*, 1360–1365. [CrossRef] [PubMed]
24. Chen, Z.; Kronawitter, C.X.; Waluyo, I.; Koel, B.E. Investigation of Water Dissociation and Surface Hydroxyl Stability on Pure and Ni-Modified CoOOH by Ambient Pressure Photoelectron Spectroscopy. *J. Phys. Chem. B* **2018**, *122*, 810–817. [CrossRef] [PubMed]
25. Zeng, Y.; Zhao, M.; Huang, Z.; Zhu, W.; Zheng, J.; Jiang, Q.; Wang, Z.; Liang, H. Surface Reconstruction of Water Splitting Electrocatalysts. *Adv. Energy Mater.* **2022**, *12*, 2201713. [CrossRef]
26. Xie, Z.; Qu, W.; Fisher, E.A.; Fahlman, J.; Asazawa, K.; Hayashi, T.; Shirataki, H.; Murase, H. Capacitance Determination for the Evaluation of Electrochemically Active Surface Area in a Catalyst Layer of NiFe-Layered Double Hydroxides for Anion Exchange Membrane Water Electrolyser. *Materials* **2024**, *17*, 556. [CrossRef] [PubMed]
27. Martínez-Hincapié, R.; Wegner, J.; Anwar, M.U.; Raza-Khan, A.; Franzka, S.; Kleszczynski, S.; Čolić, V. The determination of the electrochemically active surface area and its effects on the electrocatalytic properties of structured nickel electrodes produced by additive manufacturing. *Electrochimica Acta* **2024**, *476*, 143663. [CrossRef]
28. Poimenidis, I.A.; Lykaki, M.; Moustaizis, S.; Loukakos, P.; Konsolakis, M. One-step solvothermal growth of NiO nanoparticles on nickel foam as a highly efficient electrocatalyst for hydrogen evolution reaction. *Mater. Chem. Phys.* **2023**, *305*, 128007. [CrossRef]
29. Poimenidis, I.A.; Loukakos, P.A.; Konsolakis, M. NiO nanolayer electrodeposited with Cobalt and Phosphide as a novel supercapacitor with high areal capacitance. *J. Phys. Chem. Solids* **2025**, *196*, 112365. [CrossRef]
30. Poimenidis, I.; Skliri, E.; Binas, V.; Komnitsas, K.; Konsolakis, M. Hydrothermal growth of Co_3O_4 nanoparticles on nickel foam for high-performance pseudocapacitive supercapacitors: Effect of cobalt loading. *Next Mater.* **2026**, *10*, 101449. [CrossRef]
31. Lim, W.S.; Kim, M.H.; Park, H.J.; Lee, M.H. Characterization of Polyvinyl Alcohol (PVA)/Polyacrylic Acid (PAA) Composite Film-Forming Solutions and Resulting Films as Affected by Beeswax Content. *Polymers* **2024**, *16*, 310. [CrossRef] [PubMed]
32. Kumeta, K.; Nagashima, I.; Matsui, S.; Mizoguchi, K. Crosslinking reaction of poly(vinyl alcohol) with poly(acrylic acid) (PAA) by heat treatment: Effect of neutralization of PAA. *J. Appl. Polym. Sci.* **2003**, *90*, 2420–2427. [CrossRef]
33. Gurusamy, P.; Nagarajan, K.; Perumalsamy, S.V.; Pandian, T.; Kulandaivel, J.; Mithra, K.M.; Anand, R.; Sinthika, S. Ni/Co-doped 1T/2H MoS_2 as a robust bifunctional electrocatalyst for hydrogen and oxygen evolution in both acidic and alkaline media. *Nanoscale* **2026**, *18*, 10810–10822. [CrossRef] [PubMed]
34. Han, X.; Hu, Y.; Zhang, F.; Li, S.; Wang, W.; Wang, B.; Wang, Q. Enhanced bifunctional electrocatalysis for alkaline water splitting via NiCo alloy on nitrogen-doped carbon: Synergistically promote hydrogen and oxygen evolution reactions. *J. Mol. Struct.* **2025**, *1343*, 142834. [CrossRef]
35. Wu, J. Engineering on Ni-Co-S Bifunctional Electrocatalyst for Water-Splitting. *ECS Meet. Abstr.* **2019**, *MA2019-02*, 2110. [CrossRef]
36. Li, J.; Li, J.; Ren, J.; Hong, H.; Liu, D.; Liu, L.; Wang, D. Electric-Field-Treated Ni/Co_3O_4 Film as High-Performance Bifunctional Electrocatalysts for Efficient Overall Water Splitting. *Nano-Micro Lett.* **2022**, *14*, 148. [CrossRef]
37. Janani, G.; Yuvaraj, S.; Surendran, S.; Chae, Y.; Sim, Y.; Song, S.-J.; Park, W.; Kim, M.-J.; Sim, U. Enhanced bifunctional electrocatalytic activity of Ni-Co bimetallic chalcogenides for efficient water-splitting application. *J. Alloys Compd.* **2020**, *846*, 156389. [CrossRef]
38. Van Phuc, T.; Jana, J.; Ravi, N.; Kang, S.G.; Chung, J.S.; Choi, W.M.; Hur, S.H. Highly active Ni/Co-metal organic framework bifunctional electrocatalyst for water splitting reaction. *Int. J. Hydrogen Energy* **2022**, *47*, 22787–22795. [CrossRef]
39. Kubińska, L.; Szkoda, M.; Skorupska, M.; Grabowska, P.; Gajewska, M.; Lukaszewicz, J.P.; Ilnicka, A. Combined effect of nitrogen-doped carbon and $NiCo_2O_4$ for electrochemical water splitting. *Sci. Rep.* **2024**, *14*, 26930. [CrossRef] [PubMed]
40. Ning, Y.; Ma, D.; Shen, Y.; Wang, F.; Zhang, X. Constructing hierarchical mushroom-like bifunctional NiCo/$NiCo_2S_4$@NiCo/Ni foam electrocatalysts for efficient overall water splitting in alkaline media. *Electrochim. Acta* **2018**, *265*, 19–31. [CrossRef]
41. Tellez-Cruz, M.M.; Serrano-Lázaro, A.; Olvera, L.I.; Bizarro, M. Highly active ruthenium-cobalt oxide via spray pyrolysis as OER electrocatalyst in alkaline medium. *Int. J. Hydrogen Energy* **2025**, *168*, 150964. [CrossRef]

42. Chen, D.; Lu, R.; Pu, Z.; Zhu, J.; Li, H.-W.; Liu, F.; Hu, S.; Luo, X.; Wu, J.; Zhao, Y.; et al. Ru-doped 3D flower-like bimetallic phosphide with a climbing effect on overall water splitting. *Appl. Catal. B Environ.* **2020**, *279*, 119396. [CrossRef]
43. Wang, R.; Li, Z.; Li, Z.; Wen, M.; Wang, G.; Xie, G.; Liu, X.; Jiang, L. Electroless deposition synthesis of composite catalysts Ni-Fe-P-WO3/NF with superior oxygen evolution performance. *Int. J. Hydrogen Energy* **2022**, *47*, 29305–29314. [CrossRef]
44. Guo, Y.; Park, T.; Yi, J.W.; Henzie, J.; Kim, J.; Wang, Z.; Jiang, B.; Bando, Y.; Sugahara, Y.; Tang, J.; et al. Nanoarchitectonics for Transition-Metal-Sulfide-Based Electrocatalysts for Water Splitting. *Adv. Mater.* **2019**, *31*, 1807134. [CrossRef]